Journal of
Materials Chemistry A

PAPER

View Article Online
View Journal | View Issue

Cite this: *J. Mater. Chem. A*, 2025, **13**, 29006

Fatigue-resistant hydrogels with programmable crystalline domain crosslinking enabled by coordinated thermal-solvent strategy

Jie Wu,[ac] Jingwei Zhang,[a] Yujia Chen,[a] Wei Ji,[a] Qirui Wu[ab] and Lunhui Guan *[a]

Hydrogels are considered ideal candidates for ligament repair owing to their inherent flexibility, biocompatibility, and ease of processing. However, current hydrogel materials face critical challenges in artificial ligament applications, including insufficient strength, poor fatigue resistance, and the lack of real-time health monitoring capabilities, which severely limit their clinical use. Herein, a simple strategy for synergistically enhancing the mechanical strength of hydrogels through wet annealing and solvent exchange was developed. Wet annealing initially promotes the formation and growth of crystalline domains, while subsequent gradient solvent exchange with a deep eutectic solvent (DES) strengthens intermolecular interactions, inducing further growth of crystalline domains. As a result, a hydrogel (WE-PVA) with a high density of crystalline domains was constructed. Interestingly, WE-PVA exhibits excellent tensile strength (7.8 MPa), outstanding fatigue resistance ($\Gamma = 4210$ J m^{-2}), and long-term stability, highlighting its great potential for practical applications in artificial ligaments. Moreover, WE-PVA demonstrates remarkable sensing capabilities, enabling real-time monitoring of ligament status, further enhancing its functional value. This strategy provides a simple and versatile approach for designing hydrogels with both high strength and fatigue threshold, and holds significant promise for applications requiring superior mechanical performance.

Received 20th June 2025
Accepted 30th July 2025

DOI: 10.1039/d5ta05010c

rsc.li/materials-a

1. Introduction

As a key tissue responsible for maintaining joint biomechanical stability, ligaments are susceptible to structural damage under high-intensity mechanical loads. However, traditional artificial ligament materials are limited by insufficient biocompatibility, poor dynamic mechanical adaptability, and degradation of fatigue resistance, making it challenging to meet the clinical demands for long-term implantation.[1–4] Hydrogels, owing to their tissue-like mechanical compliance, tunable biomimetic structures, and excellent biocompatibility, have emerged as promising candidate materials for next-generation artificial ligaments.[5–11] Nevertheless, hydrogels still face inherent challenges during prolonged use, including the trade-off between strength and toughness, inadequate fatigue resistance, and poor long-term stability, severely restricting their long-term functionality.[12–16] Therefore, it is imperative to develop hydrogel materials that concurrently integrate high strength, superior toughness, excellent fatigue resistance, and long-term stability.[17–19]

Currently, establishing effective energy dissipation mechanisms within hydrogels has become a prevalent strategy to enhance the mechanical performance of polymer networks, employing approaches such as double-network construction, nanocomposite reinforcement, and anisotropic structural design.[20–24] Although these strategies can partially improve mechanical properties, traditional crosslinked networks often fail to synergistically optimize energy dissipation and structural stability, frequently leading to reduced ductility, anisotropic mechanical responses, and persistent challenges in suppressing crack propagation under cyclic loading.[25–27] Crystalline domains—highly ordered structures formed by locally aligned polymer chains within hydrogel networks—can enhance strength while maintaining flexibility, and act as physical crosslinking points to effectively impede crack propagation under prolonged stress.[28] Conventional methods for enhancing hydrogel crystallinity, such as cyclic freeze–thaw treatments and mechanically induced crystallization, are generally limited by prolonged processing times and equipment complexity.[29,30] In contrast, annealing treatments can promote crystallinity more efficiently by thermally activating polymer chain mobility to strengthen interchain interactions.[31–33] However, traditional annealing at subcritical temperatures (to avoid thermal degradation) restricts chain relaxation, preventing sufficient

---

[a] State Key Laboratory of Structural Chemistry, Fujian Key Laboratory of Nanomaterials, Fujian Institute of Research on the Structure of Matter, Chinese Academy of Sciences, Fuzhou, Fujian 350108, China. E-mail: guanlh@fjirsm.ac.cn

[b] School of Mechanical Engineering and Automation, Fuzhou University, Fuzhou 350108, China

[c] University of Chinese Academy of Sciences, Beijing, 100049, China

conformational rearrangement. Wet annealing facilitates comprehensive chain reorganization through solvent-induced activation but may result in network damage and solvent residue-induced crystalline heterogeneity. Solvent exchange, by precisely regulating interchain interactions through gradient solvent replacement, not only facilitates the formation of ordered crystalline domains but also efficiently removes residual solvents, thus offering a promising pathway for the structural optimization of annealed hydrogels.[34,35]

Herein, we propose a synergistic strengthening strategy based on wet annealing and solvent exchange to fabricate a hydrogel material (WE-PVA) with ultrahigh mechanical strength and exceptional fatigue resistance. Poly(vinyl alcohol) (PVA) was dissolved in dimethyl sulfoxide (DMSO) to form a physically crosslinked gel network. Controlled thermal fields promoted the conformational rearrangement of molecular chains, constructing a highly ordered three-dimensional network topology that enabled the oriented growth of crystalline domains. Subsequent solvent exchange further enhanced intermolecular interactions, significantly improving the size and uniformity of crystalline domains. Notably, these crystalline domains serve as dynamic physical crosslinking points, simultaneously enhancing the intrinsic strength of the material and effectively suppressing crack initiation and propagation through energy dissipation mechanisms, thus markedly improving the fatigue resistance of the WE-PVA hydrogel. Moreover, the WE-PVA hydrogel exhibited outstanding mechanical stability under prolonged cyclic loading (no crack propagation after 10 000 cycles) while maintaining stable sensing performance. Benefiting from the synergy between mechanical responsiveness and electrical sensing, the WE-PVA hydrogel achieves simultaneous long-term structural stability and real-time signal feedback under dynamic stress conditions, fulfilling the dual requirements of artificial ligaments for periodic mechanical loading and *in situ* physiological signal monitoring. Building on the synergistic wet annealing-solvent exchange strategy, this work provides an innovative material platform for developing smart artificial ligament systems with mechanical adaptivity and self-diagnostic capabilities.

2. Results and discussion

Fig. 1 illustrates the overall fabrication process of ultra-strong, fatigue-resistant PVA hydrogels using a synergistic strategy combining wet annealing and solvent exchange. In this study, PVA serves as the three-dimensional network framework, with molecular chain alignment optimized through wet annealing, and intermolecular interactions further enhanced *via* solvent exchange using a deep eutectic solvent (DES) composed of choline chloride and acrylic acid. This cooperative strategy constructs a network structure synergistically reinforced by dynamic hydrogen-bonded crosslinks and localized crystalline domains, significantly improving the mechanical strength and fatigue resistance of the hydrogel. Initially, PVA is dissolved in the highly polar solvent dimethyl sulfoxide (DMSO), where DMSO molecules disrupt the intrinsic hydrogen-bonded network by forming strong hydrogen bonds with PVA hydroxyl groups, facilitating full chain extension and uniform dispersion to form a PVA hydrogel. Subsequent wet annealing, driven by a high-temperature thermal field, induces dynamic rearrangement of the amorphous regions of PVA chains, leading to the formation of a densely crosslinked network structure and promoting crystalline domain growth. This process markedly enhances the mechanical strength and toughness of the gel, resulting in the W-PVA hydrogel. Further, a solvent exchange process progressively replaces DMSO with the DES, regulating intermolecular interactions and reinforcing the effects of wet annealing-induced chain rearrangement. Through this synergistic approach, a three-dimensional crosslinked network with high-density crystalline domains is constructed. As a result, the WE-PVA hydrogel achieves both high tensile strength and a superior fatigue threshold, attributed to the controlled crystalline domain growth and the establishment of a topological structure capable of efficient energy dissipation and crack blunting.

To systematically elucidate the effect of the reinforcement strategy on the mechanical properties of gradient polymer concentration hydrogels, uniaxial tensile tests were performed. Dumbbell-shaped specimens were used, and the tensile rate was set at 100 mm min^{-1} to ensure measurement accuracy and reproducibility. As shown in Fig. 2a–c, the tensile strength of the hydrogels increased significantly from 0.2 MPa to 2.21 MPa as the PVA content increased from 10 wt% to 20 wt%. This improvement is primarily attributed to the increased polymer network density, which enhances intermolecular interactions and imparts superior mechanical strength to the material.

In addition, the synergistic reinforcement *via* wet annealing and solvent exchange further enhanced the mechanical properties, with the tensile strength of the PVA$_{20}$ hydrogel increasing from 2.21 MPa to 7.8 MPa (WE-PVA$_{20}$). This substantial enhancement is likely due to the regulation of crystalline domain growth through the synergistic strategy, where the high-density crystalline domains act as physical crosslinking points that restrict large-scale slippage of polymer chains in the amorphous regions and efficiently transfer stress to adjacent areas, thereby significantly improving the strength of the hydrogel.[36–38] Interestingly, a 1 g sample of WE-PVA$_{20}$ was able to lift an object 5000 times its own weight without fracturing, while maintaining good elasticity, allowing for bending and twisting (Fig. 2d). Moreover, the Young's modulus and toughness of the hydrogels exhibited similar trends (Fig. 2e). The Young's modulus increased from 0.76 MPa (PVA$_{20}$) to 5.3 MPa (WE-PVA$_{20}$), and the toughness improved from 8.81 MJ m^{-3} (PVA$_{20}$) to 29.48 MJ m^{-3} (WE-PVA$_{20}$).

To further investigate the effect of the reinforcement strategy on the energy dissipation mechanism of WE-PVA$_{20}$ hydrogel, interval uniaxial cyclic loading–unloading experiments were conducted to evaluate the energy dissipation behavior under different strain conditions. The results showed that, within a strain range of 50% to 400%, the energy dissipated per cycle increased gradually from 0.5 MJ m^{-3} to 12.1 MJ m^{-3}. Notably, except for the first cycle, the energy dissipation ratio remained above 70% in each subsequent cycle, indicating that an efficient and stable energy dissipation system was constructed within

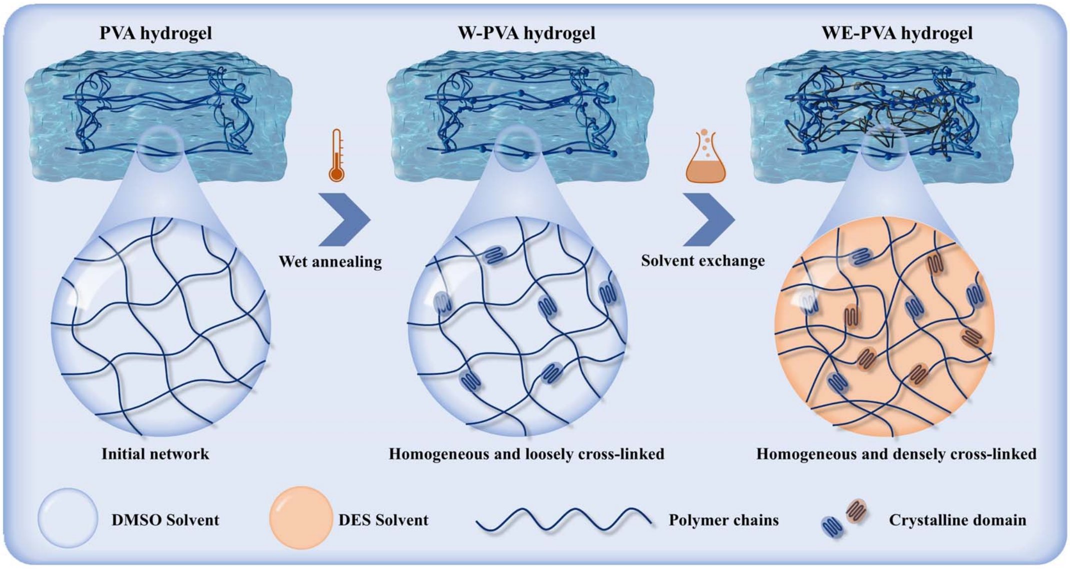

Fig. 1 Schematic illustration of the synergistic reinforcement process in PVA hydrogel *via* wet annealing and solvent exchange.

the WE-PVA$_{20}$ hydrogel (Fig. 2f–g). This behavior is likely attributed to the high-density crystalline domains acting as rigid crosslinking points, which not only limit the rebound of polymer chains and enhance the hysteresis effect, but also promote controlled slippage of polymer chains during stretching, thereby improving energy dissipation efficiency. Further cyclic tensile tests under 100% strain revealed a pronounced hysteresis phenomenon, with the hysteresis loop area gradually

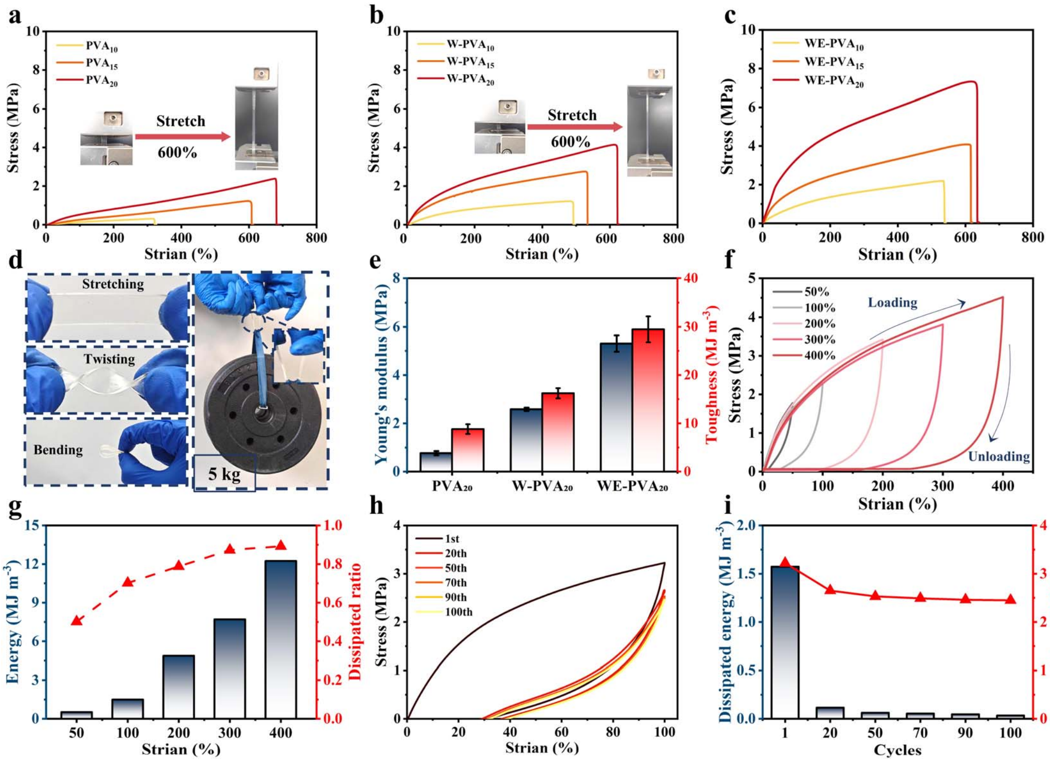

Fig. 2 Mechanical characterization of PVA$_{20}$, W-PVA$_{20}$, and WE-PVA$_{20}$ hydrogels. (a–c) Stress–strain curves of hydrogels fabricated from 10, 15, and 20 wt% PVA solutions through distinct processing routes. (d) Representative photograph of the WE-PVA$_{20}$ hydrogel. (e) Comparative Young's modulus and toughness across hydrogels. (f and g) Cyclic loading–unloading profiles of WE-PVA$_{20}$ under varying strains (50–400%), quantifying (f) dissipated energy and (g) energy dissipation ratio. (h and i) Durability assessment *via* 100 cyclic loading–unloading tests at 100% strain, tracking (h) maximum stress retention and (i) consistent energy dissipation.

decreasing with increasing cycle number. Additionally, the energy dissipated during the first cycle was significantly higher than in subsequent cycles, suggesting that certain "sacrificial bonds" within the hydrogel broke preferentially during the initial loading process, releasing energy and improving toughness (Fig. 2h). Interestingly, after 100 cycles, the WE-PVA$_{20}$ hydrogel maintained high mechanical strength, with its maximum stress decreasing only from 3.22 MPa to 2.45 MPa, corresponding to 76% retention of the initial strength (Fig. 2i). These results indicate that, despite partial damage to crosslinking points during repeated deformation, the internal network structure of the hydrogel remained stable, and it is inferred that crystalline domains, acting as crosslinking points, contributed to maintaining the overall strength of WE-PVA$_{20}$ to a certain extent. Overall, the synergistic wet annealing and solvent exchange strategy effectively enhanced both the mechanical performance and structural stability of the WE-PVA$_{20}$ hydrogel.

To elucidate the reinforcement mechanism of the hydrogel, we systematically investigated the structural evolution of the material during the strengthening process, with a focus on the synergistic regulation of molecular chain alignment and crystallization behavior by wet annealing and solvent exchange. Firstly, attenuated total reflectance Fourier transform infrared spectroscopy (ATR-FTIR) was employed to analyze the molecular interactions and their evolution within the hydrogels (Fig. S1). All three types of hydrogels exhibited a characteristic absorption peak at approximately 3270 cm^{-1}, corresponding to the stretching vibration of hydroxyl groups (–OH). Notably, compared to the PVA$_{20}$ hydrogel, the W-PVA$_{20}$ and WE-PVA$_{20}$ hydrogels displayed a slight blue shift of the hydroxyl peak, indicating enhanced hydrogen bonding interactions during the wet annealing and solvent exchange processes. This enhancement is attributed to the rearrangement and crystallization of polymer chains, which promotes redistribution and optimization of hydrogen bonds, resulting in a stronger hydrogen-bonded network within the gel.[39] X-ray diffraction (XRD) was further used to explore the changes in crystallization behavior during reinforcement (Fig. 3a). The diffraction patterns of all samples exhibited broad amorphous halo at $2\theta \approx 41.8°$, indicating the predominance of the amorphous phase. However, W-PVA$_{20}$ and WE-PVA$_{20}$ hydrogels showed more pronounced crystalline peaks compared to PVA$_{20}$. Specifically, the diffraction peak at $2\theta = 20.7°$ corresponds to the (101) plane of semi-crystalline PVA, while the shoulder at $2\theta = 24°$ is assigned to the (200) plane.[31] The emergence of these peaks provides direct evidence that wet annealing and solvent exchange significantly promote the formation of crystalline domains within the hydrogels. From a structural evolution perspective, wet annealing supplies sufficient thermal energy for molecular rearrangement of PVA chains, facilitating the development of crystalline domains. Meanwhile, solvent exchange modulates PVA chain conformation and intermolecular interactions through the introduction of new solvent molecules, promoting the formation of more stable hydrogen bonding networks and further crystal growth. To quantitatively analyze crystallinity under different conditions, differential scanning calorimetry (DSC) was performed on samples in both dry and swollen states (Fig. 3b). As shown, the crystallinity of the hydrogels significantly increased following the combined reinforcement treatment. For instance, the crystallinity of WE-PVA$_{20}$ reached 32.5% in the dry state and 7.29% in the swollen state, indicating that wet annealing and solvent exchange effectively enhance crystallization behavior, thereby improving overall crystallinity and structural stability (Fig. 3c). Scanning electron microscopy (SEM) clearly revealed the morphological characteristics of PVA$_{20}$, W-PVA$_{20}$, and WE-PVA$_{20}$ aerogels (Fig. 3d). The PVA$_{20}$ aerogel exhibited large and irregular pores with a skeleton consisting primarily of fibrous networks, indicating loosely distributed polymer chains in the untreated gel. In contrast, the W-PVA$_{20}$ and WE-PVA$_{20}$ hydrogels displayed more uniform and compact porous network structures, suggesting that the reinforcement processes facilitated polymer chain rearrangement and the formation of a denser and more uniform three-dimensional network. Small-angle X-ray scattering (SAXS) was employed to more intuitively analyze the evolution of crystalline domains during reinforcement (Fig. 3e). The 2D SAXS pattern of PVA$_{20}$ showed weak scattering signals, implying a disordered internal structure. In comparison, W-PVA$_{20}$ exhibited significantly enhanced scattering intensity, indicating that wet annealing promoted the formation and growth of crystalline domains. In the WE-PVA$_{20}$ hydrogel, well-defined diffraction rings appeared in the 2D SAXS pattern, confirming that solvent exchange further induced crystalline domain growth. As shown in the 1D SAXS profiles, the average spacing of crystalline domains decreased from 31.4 nm in PVA$_{20}$ to 23 nm in W-PVA$_{20}$ and 22.4 nm in WE-PVA$_{20}$, demonstrating that wet annealing and solvent exchange effectively increased crystalline domain density and structural order, thereby enhancing the mechanical properties of the hydrogel (Fig. 3f). The WE-PVA$_{20}$ hydrogel we prepared demonstrated a tensile strength that exceeded the values reported for similar types of hydrogels in recent years (Fig. 3g and Table S1).[40–49]

Wet annealing enhances the mobility of polymer chain segments through thermal activation, inducing chain orientation and the growth of crystalline domains. Simultaneously, solvent exchange with a deep eutectic solvent (DES) strengthens intermolecular interactions between polymer chains, further promoting the formation of crystalline domains. Together, these two processes synergistically construct a highly crystalline and structurally stable three-dimensional network. During tensile deformation, the WE-PVA$_{20}$ hydrogel exhibits a two-stage damage suppression mechanism (Fig. S2). At the initial strain stage, the densely crosslinked physical network dissipates energy primarily through controlled chain slippage and dynamic hydrogen bond breakage, while the crystalline domains serve as rigid crosslinking points to maintain network integrity. When the strain exceeds a critical threshold, crack tips propagate through the amorphous regions but are effectively blunted by the high modulus of the crystalline domains, significantly inhibiting crack extension. This hierarchical energy dissipation mechanism endows the WE-PVA$_{20}$ hydrogel with excellent crack propagation resistance.

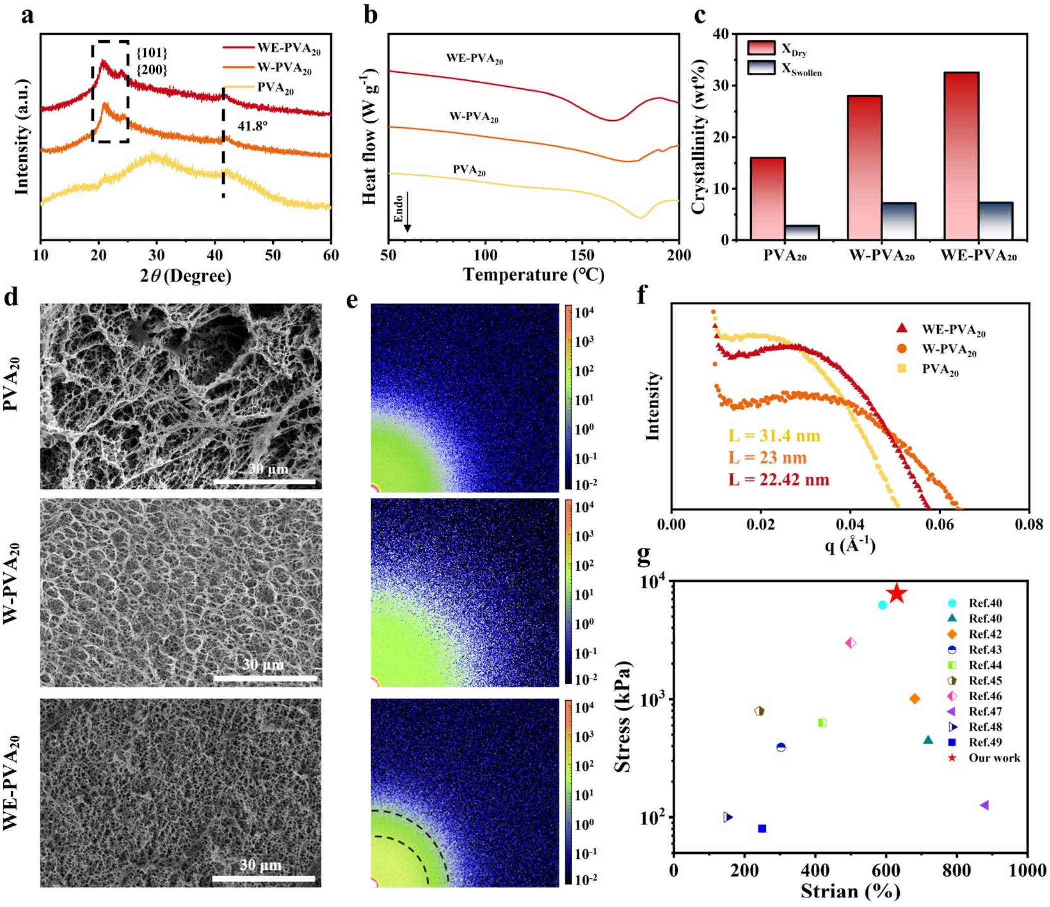

Fig. 3 Crystallization characteristics and structural evolution of hydrogels during the reinforcement process. (a) X-ray diffraction (XRD) patterns of PVA_{20}, W-PVA_{20}, and WE-PVA_{20} hydrogels. (b and c) Differential scanning calorimetry (DSC) curves and crystallinity values (dry and swollen states) for the three hydrogels. (d) SEM characterization of the three hydrogel samples. (e) Two-dimensional small-angle X-ray scattering (SAXS) patterns of the hydrogels. (f) One-dimensional SAXS profiles. (g) Comparison of the strength of WE-PVA_{20} hydrogel with that of similar hydrogels.

Material fatigue and fracture often originate from stress concentration at crack tips, which leads to uncontrolled crack propagation and ultimately results in structural failure. Therefore, the durability of hydrogels largely depends on their crack propagation resistance. To investigate the effect of the reinforcement process on the crack propagation resistance of the hydrogels, we conducted uniaxial tensile tests on samples with single-edge notches and measured their fracture energy (Fig. 4a). Experimental results showed that the untreated PVA_{20} hydrogel exhibited a fracture energy of only 5.43 kJ m^{-2}. After wet annealing, the fracture energy of W-PVA_{20} increased to 16.78 kJ m^{-2}, while the WE-PVA_{20} hydrogel, reinforced by both wet annealing and solvent exchange, demonstrated a significant enhancement, reaching 30.3 kJ m^{-2}. Furthermore, to more comprehensively evaluate the crack propagation resistance of the hydrogels, we performed trouser-tear tests to determine their tearing energy. The results exhibited a similar trend to that of the fracture energy (Fig. 4b). The tearing energies of PVA_{20}, W-PVA_{20}, and WE-PVA_{20} hydrogels were 2.8 kJ m^{-2}, 12.4 kJ m^{-2}, and 18.8 kJ m^{-2}, respectively, further confirming that the synergistic effect of wet annealing and solvent exchange effectively promotes crystalline domain growth, thereby significantly improving the material's crack propagation resistance. To quantify the fatigue resistance of the hydrogels, we applied the single-notch tensile method to determine the fatigue threshold of the WE-PVA_{20} hydrogel, which was found to be 4210 J m^{-2} (Fig. 4c). Under cyclic loading at this critical energy release rate, the notched specimen underwent 10 000 loading cycles without any observable crack growth, verifying the long-term fatigue stability of the material at the threshold level (Fig. 4d). According to fracture mechanics, the stress–strain field near the crack tip is highly concentrated, resulting in substantially larger local deformation compared to other regions. To visually observe the stress distribution during crack propagation, we employed circularly polarized light birefringence to monitor the stress state at the crack tip. As shown in Fig. 4e, when stretched to 60% strain, distinct arcuate stress concentration zones formed at the crack tips of both PVA_{20} and W-PVA_{20} hydrogels, which expanded during cyclic loading. This behavior is closely related to the insufficient suppression of crack propagation due to the sparse crystalline domains in these materials. In contrast, although stress concentration was still observed at the crack tip in the WE-PVA_{20} hydrogel, no significant crack growth occurred due to its high crystallinity and stable network structure. These

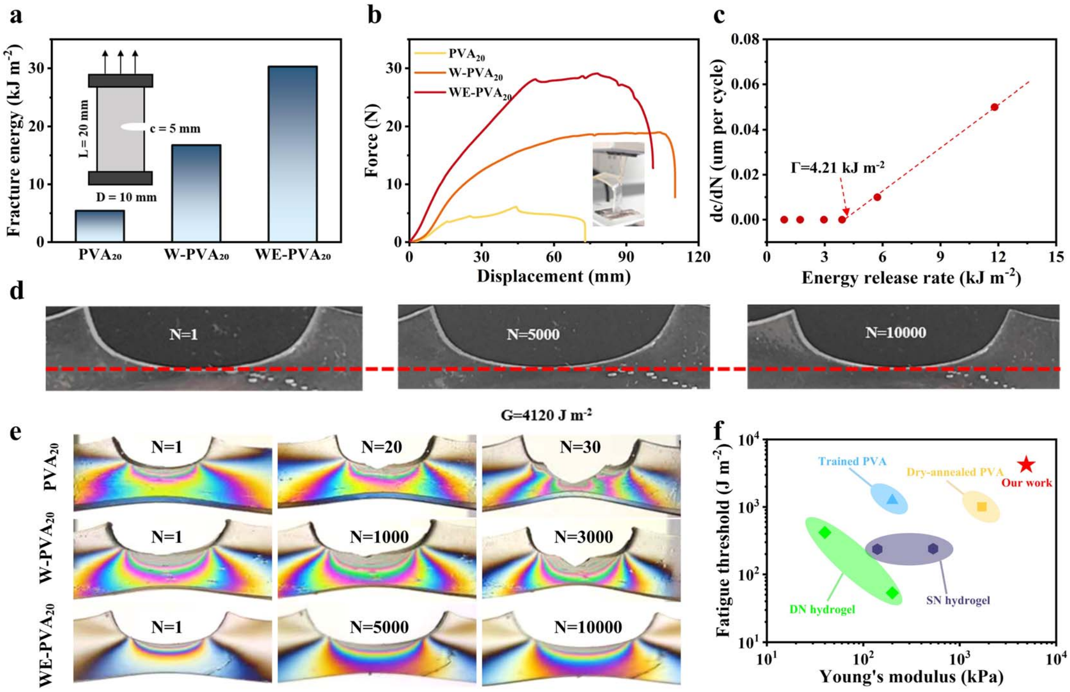

Fig. 4 Tear resistance and crack propagation behavior. (a) Fracture energy of PVA$_{20}$, W-PVA$_{20}$, and WE-PVA$_{20}$ hydrogels. (b) Tearing curves of PVA$_{20}$, W-PVA$_{20}$, and WE-PVA$_{20}$ hydrogels. (c and d) Fatigue threshold of WE-PVA$_{20}$ hydrogel and crack propagation resistance of its notched specimen over 5000 and 10 000 loading cycles (no crack propagation observed). (e) Birefringence effects of notched PVA$_{20}$, W-PVA$_{20}$, and WE-PVA$_{20}$ hydrogels during cyclic tensile testing, visualized *via* polarized light. (f) Comparison of fatigue threshold and Young's modulus of WE-PVA$_{20}$ with other reported hydrogels.

findings demonstrate that the combined treatment of wet annealing and solvent exchange significantly enhances the material's crack pinning capability by inducing the formation of high-density crystalline domains. The rigid crystalline network not only delays the accumulation of stress at the crack tip but also reduces the driving force for crack propagation through energy dissipation mechanisms, thereby imparting the material with excellent fatigue resistance. We further compared the fatigue threshold and Young's modulus of the WE-PVA$_{20}$ hydrogel with those of previously reported fatigue-resistant hydrogels (Fig. 4f and Table S2).[50–55] Within the PVA-based systems, dry-annealed PVA hydrogels, and mechanically oriented PVA hydrogels all exhibited inferior performance compared to WE-PVA$_{20}$. And the fatigue threshold of double-network hydrogels also cannot surpass the level of WE-PVA$_{20}$. Notably, WE-PVA$_{20}$ hydrogel achieves a high fatigue threshold (>4 kJ m^{-2}) while maintaining a high Young's modulus of 4.9 MPa, demonstrating its unique advantages as a biomimetic material.

Currently, the lack of effective damage monitoring methods after artificial ligament implantation leads to difficulties in timely warning of mechanical property degradation, significantly increasing the risk of implant failure. Traditional approaches are unable to capture the dynamic structural changes during material usage, making early-stage damage difficult to detect and severely compromising clinical application safety. Therefore, the development of a new generation of artificial ligaments with self-sensing capabilities, enabling real-time monitoring of structural integrity through integrated sensing modules, has become a key research direction to overcome current technical limitations. In this study, a WE-PVA$_{20}$ hydrogel-based artificial ligament with both high mechanical durability and stable electrical response was developed by utilizing the low volatility and excellent conductivity of a deep eutectic solvent (DES). Compared with conventional hydrogels, the WE-PVA$_{20}$ hydrogel designed in this work forms a stable polymer network through solvent exchange, maintaining outstanding mechanical and electrical properties even under long-term service conditions. To evaluate the sensing performance of the WE-PVA$_{20}$ hydrogel, the relationship between the relative resistance change ($\Delta R/R_0$) and tensile strain was systematically investigated (Fig. 5a). The results showed a good linear relationship between resistance change and strain (gauge factor, GF = 2.16), confirming that the material can provide stable signal output over a wide strain range. This ensures that the sensor can accurately reflect ligament deformation under various stretching states, meeting the stringent requirements for real-time monitoring in artificial ligament applications. Notably, when the stretching rate varied between 5–25 mm s^{-1}, the relative resistance change ($\Delta R/R_0$) of the hydrogel remained stable, indicating excellent resistance to strain rate interference (Fig. 5b). Further analysis demonstrated that WE-PVA$_{20}$ exhibited high sensitivity within the strain range of 50–100%, and could still detect micro-strains of 1–3% even under an extreme 300% stretch (Fig. 5c and d). This performance is attributed to the physical crosslinked network maintaining

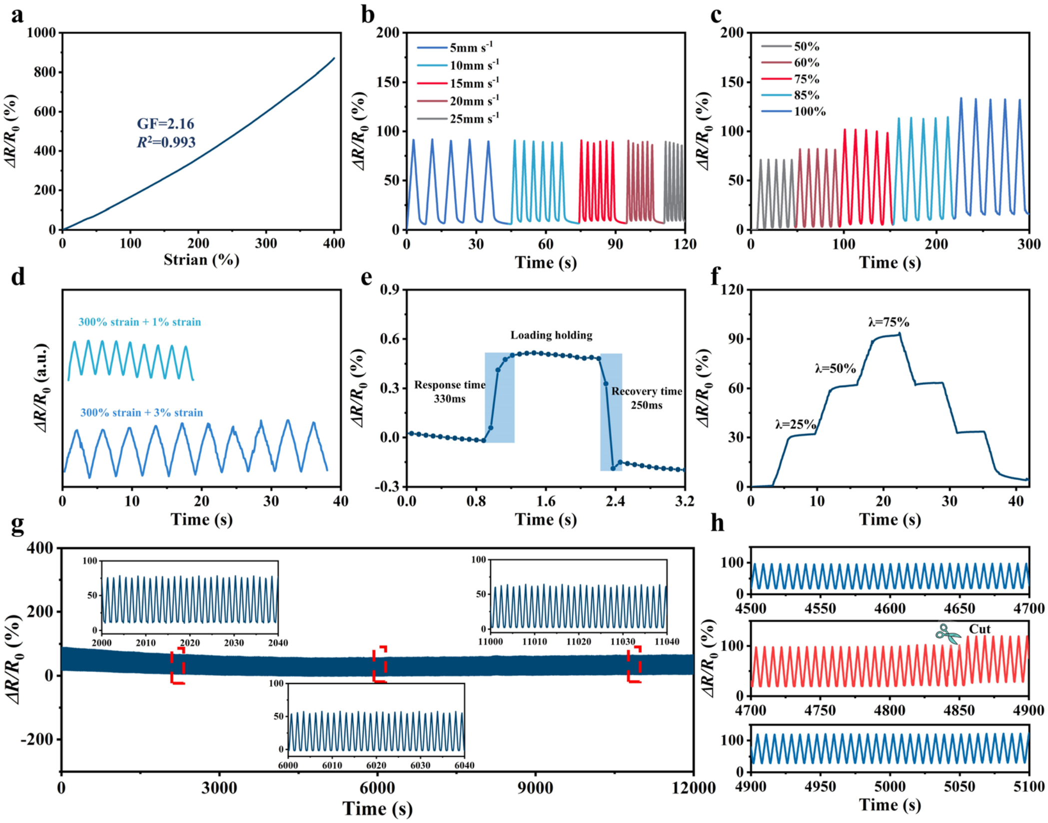

Fig. 5 Electromechanical response and sensing performance of WE-PVA$_{20}$ hydrogel. (a) Stretching sensitivity of the WE-PVA$_{20}$ hydrogel. (b and c) $\Delta R/R_0$ of the WE-PVA$_{20}$ hydrogel under different stretching rates and strains. (d) $\Delta R/R_0$ under superimposed 1% and 3% strains at a fixed 300% strain. (e) Response and recovery times of the WE-PVA$_{20}$ hydrogel during loading and unloading. (f) Stepwise tensile response of the WE-PVA$_{20}$ hydrogel. (g) $\Delta R/R_0$ over 10 000 cyclic stretching cycles at 50% strain. (h) $\Delta R/R_0$ variation of the WE-PVA$_{20}$ hydrogel after notch introduction during cyclic testing.

conductive continuity *via* ion transport pathways under external forces. The response and recovery times of the hydrogel under loading and unloading conditions were also investigated, revealing sensitive response and recovery times of 330 ms and 250 ms, respectively (Fig. 5e). In complex stepwise stretching tests, the WE-PVA$_{20}$ hydrogel stably detected resistance changes under multiple strain levels, further verifying its resistance to signal interference (Fig. 5f). These results demonstrate that WE-PVA$_{20}$ meets the dynamic monitoring requirements for artificial ligaments.

Moreover, considering that artificial ligaments in practical applications must endure a large number of repeated stretching and releasing cycles, dynamic stability and long-term reliability are critical evaluation criteria. Based on the dynamic response characteristics mentioned above, further evaluation showed that WE-PVA$_{20}$ maintained a stable $\Delta R/R_0$ signal over 10 000 cyclic stretching cycles, confirming its long-term operational reliability (Fig. 5g). To simulate clinical damage scenarios, an artificial notch was introduced during cyclic testing. As shown in Fig. 5h, the introduction of the notch caused an instantaneous increase in resistance; however, due to the crack-pinning effect of internal crystalline domains, crack propagation was effectively suppressed, and the resistance subsequently stabilized. Specifically, the WE-PVA$_{20}$ hydrogel was able to maintain basic structural integrity and provide continuous, stable electrical signals even after damage. Compared with traditional hydrogel materials, the WE-PVA$_{20}$ hydrogel demonstrates superior structural integrity and signal consistency after damage, offering a more reliable solution for real-time damage monitoring in artificial ligaments.

To validate the capability of the WE-PVA$_{20}$ hydrogel sensor for monitoring dynamic strains in artificial ligaments, a complete signal response system was established through multi-joint simulation experiments (Fig. 6a). The results demonstrated that the sensor could effectively detect various physiological activities. When attached to the elbow and finger joints, the relative resistance change exhibited a linear increase with the bending angle, and distinct signal responses corresponded to different bending angles, confirming its excellent resolution for bending amplitude (Fig. 6b and c). During wrist movement monitoring, the sensor accurately distinguished motion directions based on bidirectional resistance variations (Fig. 6d). In knee joint experiments, the signal amplitude and frequency characteristics clearly differentiated low-frequency walking from high-frequency running (Fig. 6e). To assess the biocompatibility of the WE-PVA$_{20}$ hydrogel, mouse lung epithelial cells (MLE-12 cells) were cultured on the material, and cytotoxicity was evaluated by analyzing cell viability and

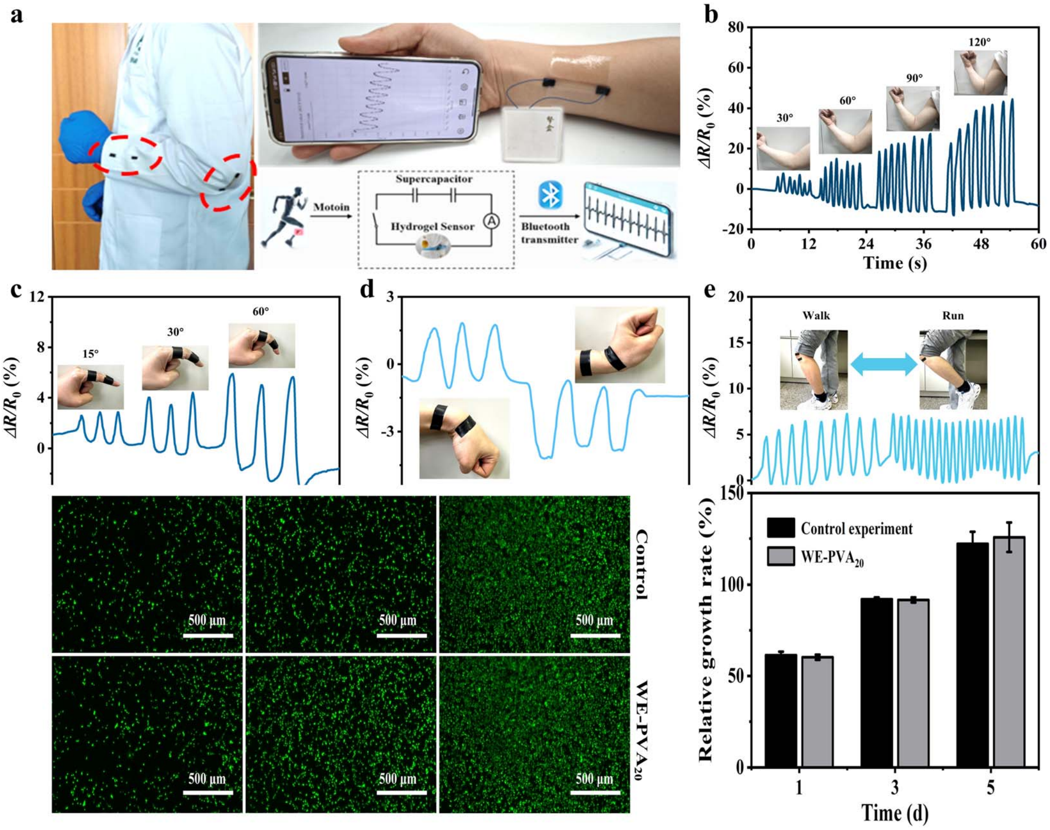

Fig. 6 Photographs and real-time resistance response curves of the WE-PVA$_{20}$ hydrogel sensor for human motion monitoring. (a) Schematic illustration of the integrated system for real-time monitoring using the WE-PVA$_{20}$ hydrogel sensor. (b) Real-time monitoring of elbow bending. (c) Real-time monitoring of finger bending. (d) Real-time monitoring of wrist bending. (e) Real-time monitoring during walking and running. (f) Fluorescence images of MLE-12 cells cultured on WE-PVA$_{20}$ hydrogel. (g) Cell viability after 1, 3, and 5 days of culture on WE-PVA$_{20}$ hydrogel.

proliferation (the control group was cultured without materials). Fluorescence microscopy revealed abundant green fluorescent live cells on all sample surfaces, indicating negligible cytotoxicity (Fig. 6f). After 5 days of culture, no significant difference in cell proliferation was observed between the WE-PVA$_{20}$ group and the control group, further confirming the hydrogel's excellent biocompatibility (Fig. 6g). Additionally, the WE-PVA$_{20}$ hydrogel was employed to simulate ligament motion. Full hydrogel samples were fixed onto a human knee joint model and subjected to bending tests, during which no visible cracks were detected; even when a pre-crack was introduced, crack propagation did not occur (Fig. S3). Collectively, these results highlight that the WE-PVA$_{20}$ hydrogel, with its high mechanical strength, outstanding fatigue resistance, excellent operational stability, and biocompatibility, provides a reliable foundation for its application as a functional material in artificial ligaments.

3. Conclusion

In summary, we successfully developed a hydrogel material with outstanding fatigue resistance through a synergistic reinforcement strategy combining wet annealing and solvent exchange. By leveraging the coordinated effects of oriented crystalline domain growth and dynamic physical crosslinking, the material exhibited high strength and exceptional structural stability, as evidenced by the absence of crack propagation in notched samples after 10 000 cycles of tensile loading. Meanwhile, the hydrogel maintained stable electrical signal feedback capabilities. These features enable real-time monitoring of structural integrity changes in artificial ligaments under dynamic loading, simultaneously meeting the dual requirements of biomechanical load-bearing and structural health monitoring. This strategy achieves integrated structural and functional design for artificial ligament materials by combining mechanical reinforcement through crystalline domains with sensing capability imparted by the deep eutectic solvent (DES), providing a new solution for the biomimetic construction of artificial ligament systems.

Conflicts of interest

There are no conflicts to declare.

Data availability

The data supporting the findings of this study are available within the article and its SI.

The file includes supplementary figures presenting additional results and corresponding FTIR spectra. See DOI: https://doi.org/10.1039/d5ta05010c.

Acknowledgements

This research was supported by National Natural Science Foundation of China (No. 22171066). The experiments on human subjects were approved informed consent.

References

1 D. Huey, J. Hu and K. Athanasiou, *Science*, 2012, **338**, 917–921.

2 S. Duan, S. Wu, M. Hua, D. Wu, Y. Yan, X. Zhu and X. He, *iScience*, 2021, **24**, 102989.

3 C. Li, R. Jia, Y. Yang and G. Liao, *Adv. Fiber Mater.*, 2023, **5**, 1549–1551.

4 H. Zhang, X. Chen, M. Ong, L. Lei, L. Zheng, B. Dai, W. Fu, J. Xu, P. Yung and L. Qin, *Engineering*, 2025, **46**, 47–59.

5 H. Zhu, C. Wang, C. Xin, Z. Dai, Y. Yang, Y. Li, M. Wang, Y. Zhang, S. Yue, R. Cai and K. Qian, *Composites, Part B*, 2025, **292**, 112068.

6 C. Yan, X. He, B. Yu, B. Zhou, S. Fang, J. Xu, B. Liu and Z. Wang, *Adv. Funct. Mater.*, 2024, **35**, 2420142.

7 Y. Ma, J. Gong, Q. Li, X. Liu, C. Qiao, J. Zhang, S. Zhang and Z. Li, *Small*, 2024, **20**, 2310046.

8 M. Li, L. Chen, Y. Li, X. Dai, Z. Jin, Y. Zhang, W. Feng, L. Yan, Y. Cao and C. Wang, *Nat. Commun.*, 2022, **13**, 2279.

9 R. Kent, A. Huang and B. Baker, *Adv. Healthcare Mater.*, 2024, **13**, 2400668.

10 H. Huang, W. Wang, Z. Liu, H. Jian, B. Xue, L. Zhu, K. Yue and S. Yang, *Small*, 2024, **20**, 2308063.

11 S. Choi, Y. Choi and J. Kim, *Adv. Funct. Mater.*, 2019, **29**, 1904342.

12 R. Bai, Q. Yang, J. Tang, X. Morelle, J. Vlassak and Z. Suo, *Extreme Mech. Lett.*, 2017, **15**, 91–96.

13 X. Li, K. Cui, T. Sun, L. Meng, C. Yu, L. Li, C. Creton, T. Kurokawa and J. Gong, *Proc. Natl. Acad. Sci. U. S. A.*, 2020, **117**, 7606–7612.

14 J. Liu, S. Lin, X. Liu, Z. Qin, Y. Yang, J. Zang and X. Zhao, *Nat. Commun.*, 2020, **11**, 1071.

15 W. Zhang, X. Liu, J. Wang, J. Tang, J. Hu, T. Lu and Z. Suo, *Eng. Fract. Mech.*, 2018, **187**, 74–93.

16 D. Ji, T. Nguyen and J. Kim, *Adv. Funct. Mater.*, 2021, **31**, 2101095.

17 Z. Xu, Y. Yang, X. Pang, B. Jiang, P. Mao, L. Gong, B. Wang, L. Peng, L. Tang and S. Li, *Chem. Eng. J.*, 2025, **503**, 158243.

18 Z. Xu, Y. Yang, X. Pang, Y. Xu, L. Gong, L. Tang and S. Li, *J. Mater. Sci. Technol.*, 2025, **237**, 10–19.

19 Z. Zeng, Y. Yang, X. Pang, B. Jiang, L. Gong, Z. Liu, L. Peng and S. Li, *Adv. Funct. Mater.*, 2024, **34**, 2409855.

20 K. Cui and J. Gong, *Aggregate*, 2021, **2**, e33.

21 J. Gong, *Soft Matter*, 2010, **6**, 2583–2590.

22 J. Gong, Y. Katsuyama, T. Kurokawa and Y. Osada, *Adv. Mater.*, 2003, **15**, 1155–1158.

23 M. Hua, S. Wu, Y. Ma, Y. Zhao, Z. Chen, I. Frenkel, J. Strzalka, H. Zhou, X. Zhu and X. He, *Nature*, 2021, **590**, 594–599.

24 H. Huang, Z. Dong, X. Ren, B. Jia, G. Li, S. Zhou, X. Zhao and W. Wang, *Nano Res.*, 2023, **16**, 3475–3515.

25 W. Li, X. Wang, Z. Liu, X. Zou, Z. Shen, D. Liu, L. Li, Y. Guo and F. Yan, *Nat. Mater.*, 2023, **23**, 131–138.

26 W. Li, S. Zheng, X. Zou, Y. Ren, Z. Liu, W. Peng, X. Wang, D. Liu, Z. Shen, Y. Hu, J. Guo, Z. Sun and F. Yan, *Adv. Funct. Mater.*, 2022, **32**, 2207348.

27 W. Li, L. Li, S. Zheng, Z. Liu, X. Zou, Z. Sun, J. Guo and F. Yan, *Adv. Mater.*, 2022, **34**, 2203049.

28 L. Xu, Y. Qiao and D. Qiu, *Adv. Mater.*, 2023, **35**, 2209913.

29 H. Adelnia, R. Ensandoost, S. Shebbrin Moonshi, J. Gavgani, E. Vasafi and H. Ta, *Eur. Polym. J.*, 2022, **164**, 110974.

30 M. Mredha, Y. Guo, T. Nonoyama, T. Nakajima, T. Kurokawa and J. Gong, *Adv. Mater.*, 2018, **30**, 1704937.

31 N. Tang, Y. Jiang, K. Wei, Z. Zheng, H. Zhang and J. Hu, *Adv. Mater.*, 2023, **36**, 2309576.

32 Z. Liu, H. Zhang, R. Zhou, H. Gao, Y. Wu, Y. Wang, H. Wu, C. Guan, L. Wang, L. Tang, P. Song, H. Xue and J. Gao, *Adv. Sci.*, 2025, **12**, 2414339.

33 Y. Sun, Y. Xie, H. Zou, Y. Chen, Z. Wen, Q. Liang, X. Peng, J. Sui, J. Chen, Y. He, Y. Wu, L. Guo, G. Wang, G. Zang and Y. Zhang, *Chem. Eng. J.*, 2024, **495**, 153487.

34 Y. Wu, Y. Zhang, H. Wu, J. Wen, S. Zhang, W. Xing, H. Zhang, H. Xue, J. Gao and Y. Mai, *Adv. Mater.*, 2023, **35**, 2210624.

35 L. Xu, S. Gao, Q. Guo, C. Wang, Y. Qiao and D. Qiu, *Adv. Mater.*, 2020, **32**, 2004579.

36 W. Lian, Z. Fan, K. Cui, P. Yin, J. Yang, H. Jiang, L. Tang and T. Sun, *Macromolecules*, 2021, **54**, 8996–9006.

37 K. Song, M. Zhang, J. Han, M. Chen, J. Xu, Y. Yin, Z. Li and D. Liu, *Macromolecules*, 2025, **5**, 3509–3519.

38 F. Wu, J. Gao, Y. Xiang and J. Yang, *Polymers*, 2023, **15**, 3782.

39 S. Du, X. Chen, M. Li, B. Peng, Q. Lyu, L. Zhang and J. Zhu, *Adv. Funct. Mater.*, 2024, **35**, 2409726.

40 Y. Huang, P. Shen, Q. Ma, W. Li, N. Ma, X. Wang, B. Sun, F. Xia, Y. Jiang and M. Zhu, *Nano Energy*, 2025, **138**, 110898.

41 Z. Wu, L. Zhang, M. Wang, D. Zang, H. Long, L. Weng, N. Guo, J. Gao, Y. Liu and B. Xu, *Adv. Compos. Hybrid Mater.*, 2025, **8**, 17.

42 J. Wang, Q. Shao, W. Wang, Z. Ma, L. Wu, R. Song, H. Liang, Y. Dong, M. Tahir, Z. Hu, X. Huang and L. He, *Chem. Eng. J.*, 2024, **498**, 155679.

43 S. Entifar, N. Entifar, A. Wibowo, J. Kim, Y. Sembiring, J. Saputro, H. Kim, J. Kim, G. Xie, J. Oh, S. Kim, D. Lim, M. Moon, M. Kim and Y. Kim, *Chem. Eng. J.*, 2025, **509**, 160971.

44 M. Gong, X. Wang, Z. Wu, L. Yue, Q. Chen, H. Li, X. Lin, L. Zhang and D. Wang, *Small*, 2024, **20**, 2400161.

45 J. Hu, Y. Wu, Q. Yang, Q. Zhou, L. Hui, Z. Liu, F. Xu and D. Ding, *Carbohydr. Polym.*, 2022, **275**, 118697.

46 R. Karyappa, N. Nagaraju, K. Yamagishi, X. Koh, Q. Zhu and M. Hashimoto, *Mater. Horiz.*, 2024, **11**, 2701–2717.

47 K. Qian, J. Zhou, M. Miao, S. Thaiboonrod, J. Fang and X. Feng, *Composites, Part B*, 2024, **287**, 111826.

48 Y. Zhang, Y. Xiong, X. Li, S. Zhang, W. Xu, H. Chen and L. Xu, *Adv. Funct. Mater.*, 2024, **35**, 2415207.

49 W. Zhao, H. Zhou, W. Li, M. Chen, M. Zhou and L. Zhao, *Nano-Micro Lett.*, 2024, **16**, 99.

50 S. Lin, X. Liu, J. Liu, H. Yuk, H. Loh, G. Parada, C. Settens, J. Song, A. Masic, G. McKinley and X. Zhao, *Sci. Adv.*, 2019, **5**, aau8528.

51 R. Bai, Q. Yang, J. Tang, X. Morelle, J. Vlassak and Z. Suo, *Extreme Mech. Lett.*, 2017, **15**, 91–96.

52 S. Lin, J. Liu, X. Liu and X. Zhao, *Proc. Natl. Acad. Sci. U. S. A.*, 2019, **116**, 10244–10249.

53 X. Li, K. Cui, T. Kurokawa, Y. Ye, T. Sun, C. Yu, C. Creton and J. Gong, *Sci. Adv.*, 2021, **7**, abe8210.

54 J. Kim, G. Zhan, M. Shi and Z. Suo, *Science*, 2021, **374**, 212–216.

55 W. Zhang, X. Liu, J. Wang, J. Tang, J. Hu, T. Lu and Z. Suo, *Eng. Fract. Mech.*, 2018, **187**, 74–93.